Influence of atomization quality modulation on flame dynamics in a hypergolic rocket engine

Moritz Schulze, Martin Schmid and Thomas Sattelmayer

Abstract

For the numerical evaluation of the thermoacoustic stability of rocket engines often hybrid methods are applied, which separate the computation of wave propagation in the combustor from the analysis of the flame response to acoustic perturbations. Closure requires a thermoacoustic feedback model which provides the heat release fluctuation in the source term of the employed wave transport equations. The influence of the acoustic fluctuations in the combustion chamber on the heat release fluctuations from the modulation of the atomization of the propellants in a hypergolic upper stage rocket engine is studied. Numerical modeling of a single injector provides the time mean reacting flow field. A network of transfer functions representing all aspects relevant for the feedback model is presented. Analytical models for the injector admittances and for the atomization transfer functions are provided. The dynamics of evaporation and combustion are studied numerically and the numerical results are analyzed. An analytical approximation of the computed flame transfer function is combined with the analytical models for the injector and the atomization quality to derive the feedback model for the wave propagation code. The evaluation of this model on the basis of the Rayleigh index reveals the thermoacoustic driving potential originating from the fluctuating spray quality.

Introduction

Under unfavorable conditions, the interaction of the combustor chamber acoustics with the reacting flow field and with the propellant feed system leads to extremely high-pressure fluctuations in rocket engines, which result in high mechanical stress and an increase of the heat flux to the combustion chamber walls. These high mechanical and thermal loads can cause serious structural damage of the combustion chamber and, in the worst case, the fast destruction of the rocket engine. For this reason, the verification of thermoacoustic stability is one of the main requirements during the development of liquid rocket engines. The prediction of high-frequency oscillations (HF) is particularly challenging, because they usually exhibit significantly lower nozzle damping than longitudinal modes.[1]

Several numerical tools have become available for the investigation of thermoacoustic instabilities. Most of them model the thermoacoustic feedback provided by flame dynamics separately from the wave propagation in the combustion chamber.[2–9] The separated determination of flame dynamics and wave propagation is necessary, since state of the art computational fluid dynamics (CFD) tools are not capable of providing fully discretized simulations of realistic rocket engine configurations including a high number of injectors over acoustically relevant time spans. Single injector investigations, however, allow for detailed studies on combustion processes and parameter variations are possible. Furthermore, amplitude dependent analysis

Lehrstuhl für Thermodynamik, Technische Universität München, Boltzmannstraße, Garching b. München, Munich, Germany

Corresponding author:
Moritz Schulze, Lehrstuhl für Thermodynamik, Technische Universität München, Boltzmannstraße 15, 85748 Garching b. München, Munich, Germany.
Email: schulze@td.mw.tum.de

can be conducted. Consequently, the derivation of feedback models can be based on physically motived mechanisms. Typically, HF instabilities in rocket engines are characterized by the first transverse mode with longitudinal components originating from the admittances of the injector plate and the nozzle and from convection in the combustor. This allows the numerical computation of flame dynamics on the basis of single injector numerical modeling,[2] which finally must be cast in feedback models for the wave propagation code to provide access to the evaluation of rocket engine combustion stability.[2–5,10] The description of acoustic propagation within the entire thrust system is then based on linearized equations, which reduce computational efforts substantially. Stability ratings based on linear equations, however, state only the linear stability, i.e. initial growth rates of potentially unstable load points. Limit cycle amplitudes, which are defined by non-linear saturation effects, cannot be predict. Non-linear acoustic wave propagation is possible to consider but increase turnaround times again.

Acoustic modes always consist of a superposition of pressure and velocity fluctuations. These interact with the processes that take place from the injection of the propellants to their complete combustion. In addition to the direct influences of the acoustic velocity and the pressure on flame dynamics, there are additional effects caused by the acoustic excitation of the injector flow. Recently, the impact of acoustically triggered propellant mass flow oscillations in the injectors on the vaporization and hence heat release rate fluctuations is investigated in Sattelmayer et al.[11] These studies impose a constant distribution of droplets the injector outlet, which is not varied in time. The influence of acoustics on atomization is excluded intentionally. In hypergolic rocket engines, however, the modulation of the atomization quality is an additional effect originating from pulsating mass flows in the injector. The investigation of the relevance of atomization quality fluctuations on flame dynamics is in the focus of the numerical single injector study presented below. The studied configuration provided by *Airbus Defence and Space* is a rocket engine propelled with Monomethylhydrazine (CH_6N_2, MMH) and Nitrogen tetroxide (N_2O_4, NTO).[2,11]

In the "Introduction" section, the investigated configuration and the employed numerical approach are presented before the steady state results are discussed for illustration of the mixture preparation and the flame shape. Subsequently, the framework of transfer functions is introduced, which provides the basis for the flame feedback model required for the wave propagation code. Analytical submodels for the injector dynamics and the atomization quality fluctuations are derived, which link the temporal modulation of the spray quality to the acoustic pressure downstream of the faceplate of the rocket engine. In the following sections, numerical computations with imposed droplet diameter fluctuations are presented. These computations reveal the dynamics of the evaporation of both propellants and the heat release in the flame. Subsequently, an analytical feedback model is provided. Finally, the thermoacoustic driving potential of spray quality fluctuations is assessed.

Configuration and computational method

A rocket engine configuration developed at *Airbus Defence and Space* which uses MMH and NTO as liquid propellants is considered in the numerical study presented below. The employed design is typical for upper stage engines, which are usually operated at moderate pressure.

The computational domain is reduced to one single injector, see Figure 1. The corresponding reduced chamber radius is given by $R^\star \approx 10$ mm and is scaled such that the area ratio between injection area of the propellants and chamber cross-section is conserved. In the following, the geometrical dimensions are presented in dimensionless form using $R^\star$ as reference.

In addition, the propellant injection system is also shown in Figure 1. To match experimental injection conditions accurately and at the same time to keep computational efforts within reasonable limits, a special treatment of the inlet conditions is applied, in which the injection geometry is not entirely resolved. The swirling flow of NTO is injected through an annular area with a radius of $\tilde{R}_{o,N} = 0.099$ in the center. Due to the swirl of the NTO flow, a stagnation region in the center of the injection area establishes, yielding an annular injection region (see Figure 1) with an inner radius of the annular injection region of $\tilde{R}_{o,N} = 0.066$. A linear distribution of the radial injection angle of the NTO flow is assumed ($\alpha_i < \alpha < \alpha_a$). The injection velocity, $u_{Inj,N}$, however, is set constant over the entire injection area (see also Table 1), leading to an increasing radial velocity component in radial direction. The swirl of the NTO flow generates a circumferential velocity component, u_Θ, which is assumed to be independent of the radius. In the engine, the MMH flow is axially injected through 12 radially oriented slits with an outer radius of $\tilde{R}_{o,M} = 0.26$ and disintegrates downstream of the slits into droplets. In the numerical computations, however, the MMH droplets are injected with a homogeneously distributed velocity $u_{Inj,M}$ through the surface of several truncated cones with an opening angle of $5°$ and with the base being located at the slits. The circular base diameter of the cones corresponds to the slit width. Altogether four cones are necessary per slit to represent the injection area for MMH, see Figure 1. In order to
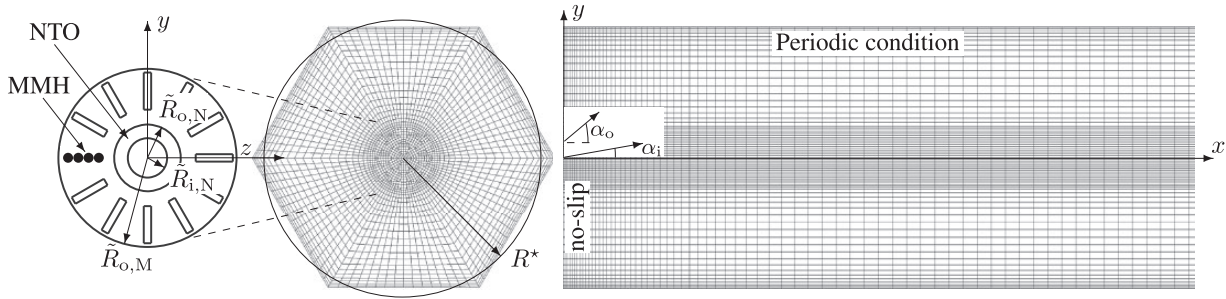
Figure 1. MMH and NTO injection (left), numerical grids in y-z plane (middle), and upstream part of the grid in the x-y plane (right). Injection angles of NTO at $\tilde{R}_{\mathrm{i,N}}$ and $\tilde{R}_{\mathrm{o,N}}$ (right). MMH: monomethylhydrazine; NTO: nitrogen tetroxide.

Table 1. Operating point and injection conditions.

$\bar{p}$	[bar]	11	
O/F	[−]	2.05	
		MMH	NTO
$\dot{M}$	[g/s]	23.2	47.5
D_{RR}	[μm]	15	20
N		3	3
u_{Inj}	[m/s]	42	66
α_{i}	[°]		5
α_{a}	[°]		38
u_{Θ}	[m/s]		5

MMH: monomethylhydrazine; NTO: nitrogen tetroxide.

achieve sufficient dispersion of the MMH spray, an angle of $5°$ is assumed for the initial MMH droplet trajectories with respect to the x-direction. Both MMH and NTO are injected at a temperature of 300 K. To gain representative computational field results, 3000 droplet trajectories are calculated for both propellants per run.

The investigated point of operation and the selected injection conditions are given in Table 1. As the stoichiometric oxidizer to fuel ratio O/F for MMH and NTO is 2.5, the rocket engine is operated at overall fuel rich condition with approximately 20% fuel overshoot.

According to the experience with numerical simulations of the selected configuration, the injection velocities $\left(u_{\mathrm{Inj}}, u_{\Theta}\right)$ and angles $\left(\alpha_{\mathrm{i}}, \alpha_{\mathrm{a}}\right)$ are representative for the injection technology employed in the considered engine design. The droplet sizes follow a Rosin–Rammler distribution according to Lefebvre,[12] which yields for the volume-based distribution of the droplet diameters:

$$f_{\mathrm{V}}(D_{\mathrm{D}}) = \frac{n}{D_{\mathrm{D}}} \cdot \left(\frac{D_{\mathrm{D}}}{D_{\mathrm{RR}}}\right)^{n} \cdot \exp\left(-\left(\frac{D_{\mathrm{D}}}{D_{\mathrm{RR}}}\right)^{n}\right) \quad (1)$$

where D_{RR} denotes the characteristic mean droplet diameter, D_{D} the droplet diameter, and n an exponent. An appropriate choice of the parameters has been found through testing and validation on experimental findings on the basis of chamber pressure and optical visualizations. The exponent n is set to three for all load points and the characteristic diameters of the droplet distributions are reported in Table 1. The corresponding volume-based distributions of droplet diameters D_{D} for $D_{\mathrm{RR}} = 15\,\mu$m and $20\,\mu$m are shown in Figure 2.

As it can be seen, the location of the peak values tends towards higher droplet diameters with increasing mean diameter. Moreover, the spreading of the distribution is larger for higher mean diameters. To gain representative computational field results, 3000 droplet trajectories are calculated for both propellants per run. Herein a certain number of physical droplets are combined to one numerical droplet to reduce numerical cost.

For the numerical investigation of the modulation of atomization quality on flame dynamics, the unsteady RANS method on the basis of the commerical CFD solver ANSYS CFX 14.0 is employed. A thorough evaluation of discretization, convergence, and time stepping led to the selection of first-order spatial and temporal discretization with approximately 450,000 elements and a time step of $2 \cdot 10^{-5}$ s. The combustion process including the dynamics of the liquid droplets, evaporation, mixing as well as combustion is modeled on the basis of a coupled Euler–Lagrange method. Both propellants are injected as liquid droplets with a well-defined size distribution. In the Lagrangian frame of reference, the trajectories of the droplets are calculated and source terms regarding mass, momentum, and energy for the transformation into the gas phase are determined. The gas phase, in turn, is described in the Eulerian frame of reference using the Shear Stress Transport model to account for turbulence.

Evaporation of the liquid phase and hence the source terms of energy and mass for the gas phase is based on an infinite conductivity model providing infinitely fast thermal mixture by diffusion and convection inside of a droplet yielding a constant temperature.
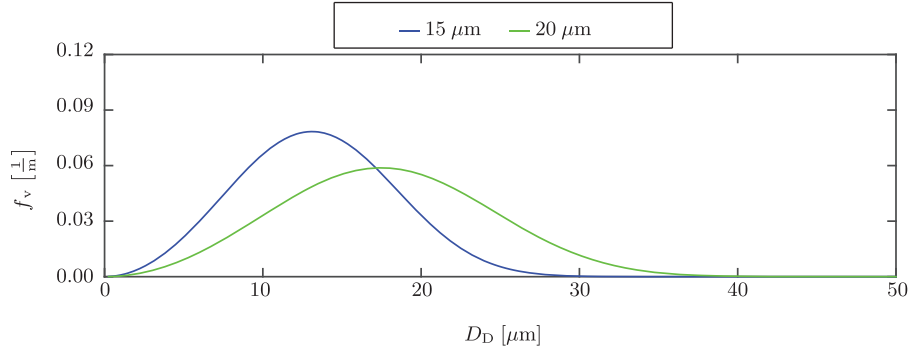
Figure 2. Rosin–Rammler distribution for different characteristic mean droplet diameters, D_{RR}.

This droplet temperature T_D may vary in time and results from the equilibrium of heat flow from the environment to the droplet and enthalpy of vaporization. The convective heat transfer is given by

$$\dot{Q}_c = \pi \cdot D_D \cdot \lambda_Q \cdot \text{Nu} \cdot (T - T_D) \quad (2)$$

where λ_Q denotes heat conductivity and the Nusselt number is given by

$$\text{Nu} = 2 + 0.6 \cdot \text{Re}^{1/2} \cdot \text{Pr}^{1/3} \quad (3)$$

The enthalpy flow due to evaporation is given by

$$\dot{Q}_v = \frac{dM_D}{dt} \cdot h_v \quad (4)$$

where h_v states the enthalpy of vaporization and M the droplet mass. The change of droplet temperature is given by

$$M_D \cdot c_{p,D} \cdot \frac{dT_D}{dt} = \dot{Q}_c + \dot{Q}_v \quad (5)$$

The film evaporation model is used to describe the change of droplet temperature:

$$\frac{dM_D}{dt} = \pi \cdot D_D \cdot \rho \cdot D_F \cdot \text{Sh} \cdot \frac{W_i}{W_G} \cdot \ln\left(\frac{1 - \chi_s}{1 - \chi_v}\right) \quad (6)$$

where W_i and W_G denote the molecular weights of the i-th vaporizing species and of the mixture of the continuous phase. The Sherwood number reads

$$\text{Sh} = 2 + 0.6 \cdot \text{Re}^{0.5} \cdot \left(\frac{\mu}{\rho \cdot D_F}\right)^{\frac{1}{3}} \quad (7)$$

where Re denotes the Reynolds number, μ dynamic viscosity, ρ density, and D_F diffusivity. Furthermore, χ_v states the mole fraction of the vaporizing species in the circumfluent gas and χ_s the equilibrium mole

Table 2. Parameter of Antoine equation.

	Unit	MMH	NTO
p_{sc}	Pa	1.0000 E + 00	1.0000 E + 00
A	–	2.3591 E + 01	2.5711 E + 01
B	K	4.3845 E + 03	4.3843 E + 03
C	K	2.1228 E + 00	1.4477 E + 01

MMH: monomethylhydrazine; NTO: nitrogen tetroxide.

fraction of the vaporizing species on the droplet surface, which is given by

$$\chi_s = \frac{p_v}{p} \quad (8)$$

The vapor pressure is given by the Antoine equation, which reads

$$p_v = p_{sc} \cdot \exp\left(A - \frac{B}{T_D + C}\right) \quad (9)$$

The parameters of the Antoine equation for MMH and NTO are given in Table 2.

The source terms of energy and mass for the gas phase can finally be determined from equations (5) and (6). The chemical reactions are modeled through a combination of an Eddy Dissipation Concept and a Finite-Rate approach, see ANSYS.[13] The conversion from MMH/NTO into the products is assumed to be fully controlled by turbulent mixing and kinetics are not a limiting factor. The assumption is based on the high reactivity of the hypergolic propellant combination MMH/NTO. Hypergolic propellants react spontaneously without the addition of ignition energy and only mixing is the limiting parameter. The global reaction
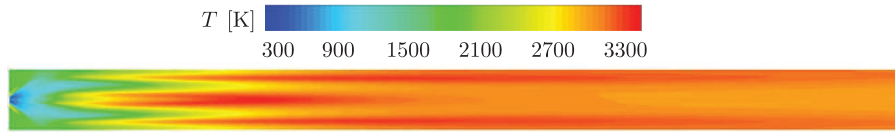
$$CH_6N_2 + 1.15\,N_2O_4 \rightarrow 0.4\,CO + 0.6\,CO_2 \\ + 3.0\,H_2O + 2.15\,N_2, \quad (10)$$

$$T \ [\mathrm{K}]$$
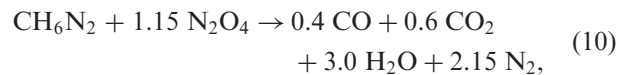
Figure 3. Steady temperature field.

is applied, which leads to the i-th (Y_i) source term

$$\dot{\omega}_{Y_i} = \left(\nu_i'' - \nu_i'\right) \cdot \rho \cdot W_i \cdot A_{\mathrm{EDC}} \cdot \frac{\epsilon}{k_t} \cdot \min\left(\frac{Y_R}{\nu_R' \cdot W_R}\right) \tag{11}$$

In addition, the dissociation of water is incorporated in order to obtain realistic flame temperatures. The dissociation reaction is given by

$$\mathrm{H_2O} \rightarrow \mathrm{OH} + \mathrm{H} \tag{12}$$

and is assumed to be kinetically controlled, which leads to the i-th (Y_i) source term.[14]

$$\dot{\omega}_{Y_i} = \left(\nu_i'' - \nu_i'\right) \frac{\rho \cdot Y_{\mathrm{H_2O}}}{W_{\mathrm{H_2O}}} W_i A_{\mathrm{FR}} T^{\beta_{\mathrm{FR}}} e^{-\frac{E_{\mathrm{FR}}}{\mathcal{R} T}} \tag{13}$$

with the constants $A_{\mathrm{FR}} = 3.5 \cdot 10^9 \ \mathrm{s}^{-1}$, $\beta_{\mathrm{FR}} = 0$, and $E_{\mathrm{FR}}/\mathcal{R} = 52900\mathrm{K}$. The introduced dissociation reaction describes the total decomposition of water. Further reactions of OH and H are not included, which is, considering the high temperatures, a reasonable assumption. A more detailed description of the numerical model is given in Schmid.[2] The applicability of the model for the simulation of MMH and NTO combustion has been demonstrated by several authors in the past.[14–17]

In axial direction, the computational domain comprises the distance from the injection plane to approximately the nozzle throat plane. The nozzle, however, is not included in the simulation. The grid resolution in axial direction is shown in Figure 1. To reflect the influence of neighboring injectors, periodic conditions are applied at the corresponding boundaries. Instead of a circular domain, a hexagonal cross-section is used to achieve well-defined periodicity, while the area of the cross-section is conserved. The grid resolution in the y-z plane is also shown in Figure 1. The injection plane is treated as no-slip wall for the gas phase. At the outlet, the pressure is set according to Table 1.

The steady computation based on the input data listed in Table 1 results in the temperature field in the longitudinal mid plane (x-y plane) shown in Figure 3.

The minimum temperature is in the range of 300 K, which corresponds to the injection temperature of the liquid propellants. The maximum temperature is
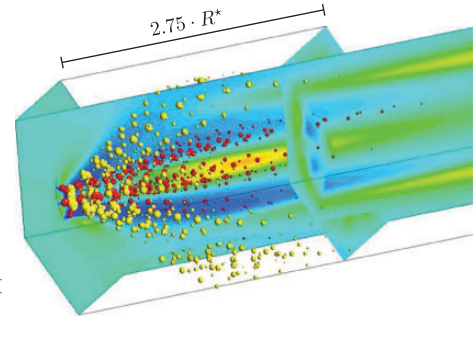

Figure 4. Droplet trajectories of MMH and NTO. MMH: monomethylhydrazine; NTO: nitrogen tetroxide.

approximately 3300 K. This represents a good approximation of the equilibrium temperature of these fuels in the considered pressure and mass flow ranges. A cone-shaped flame can be recognized clearly that is dominated in the upstream part by the evaporation of the propellants and further downstream through the diffusion of the gaseous propellants. Similarly, another region of high temperature forms in the center near the injector. It occurs in the shear layer of gaseous MMH and NTO.

Figure 4 shows the droplet trajectories of MMH (red) and NTO (yellow). The planes are color-coded with the temperature level and only the area close to the injection plane is shown. The size of the spheres is proportional to the droplet diameter. Because the MMH droplets are injected in axial direction, almost no radial dispersion of the MMH spray is observed in the evaporation zone and the MMH droplet trajectories remain almost axial. However, due to the swirl imposed on the NTO, the NTO droplets move significantly stronger outward than the MMH droplets. This leads to an interpenetration of both droplet clouds. Near the injector, higher temperatures (yellow-orange zone) in the gas phase are only observed near the axis, whereas the temperatures remain low in the two conical zones, where one of both propellant sprays dominates (blue zone). In axial direction evaporation is completed at $x/R^\star \approx 4$.

If the evaporation times are determined from the simulations for all individual droplets, continuous distributions around characteristic mean values are obtained. The mean values for the investigated operating point are given in Table 3. The pseudo frequencies

in Table 3 correspond to the inverse of the respective mean evaporation times. This shows that the evaporation time is in the range of typical inverse HF instability frequencies and that the acoustic fluctuations may have a significant impact on the coupling mechanisms originating from the modulation of evaporation.

Impact of acoustics on mixture preparation and combustion

Governing effects

Upon injection of the liquid propellants into the combustion chamber, the fuel and oxidizer jets begin to disintegrate due to shear forces between the liquid and gaseous phase, which are determined in particular

Table 3. Mean evaporation time and frequency.

		MMH	NTO
$\bar{\tau}_v$	[ms]	0.36	0.24
$\bar{\tau}_v^{-1}$	[Hz]	2770	4174

MMH: monomethylhydrazine; NTO: nitrogen tetroxide.

by their relative velocity.[18,19] Atomization is further supported by turbulence generated in the fuel and oxidizer flow in the injector. And in the investigated configuration, the axial injection of MMH and the conical injection of NTO (see Figure 4) lead to impingement of the liquid jets, which intensifies liquid disintegration and spray formation.

The modulation of atomization quality by acoustic fluctuations has been studied experimentally by several authors,[20–22] but the investigated injector types and frequency ranges are considerably different from the configuration of current interest.

Figure 5 schematically shows how acoustic fluctuations affect atomization, evaporation, and heat release. The first direct influence of the acoustic field on the modulation of the atomization quality originates from the temporal changes of the relative velocity between the liquid and gas phase represented by the acoustic velocity fluctuations in axial direction $\hat{u}$ and transverse direction $\hat{w}$. The second influence is caused by the dynamic pressure field near the injector exit ($\hat{p}$), which modulates the injection velocities $\hat{u}_{M,fl}$ and $\hat{u}_{N,fl}$ of the two liquids. Regardless of whether fluctuating injection velocities or relative velocities in the chamber are considered, the consequence is always a temporarily
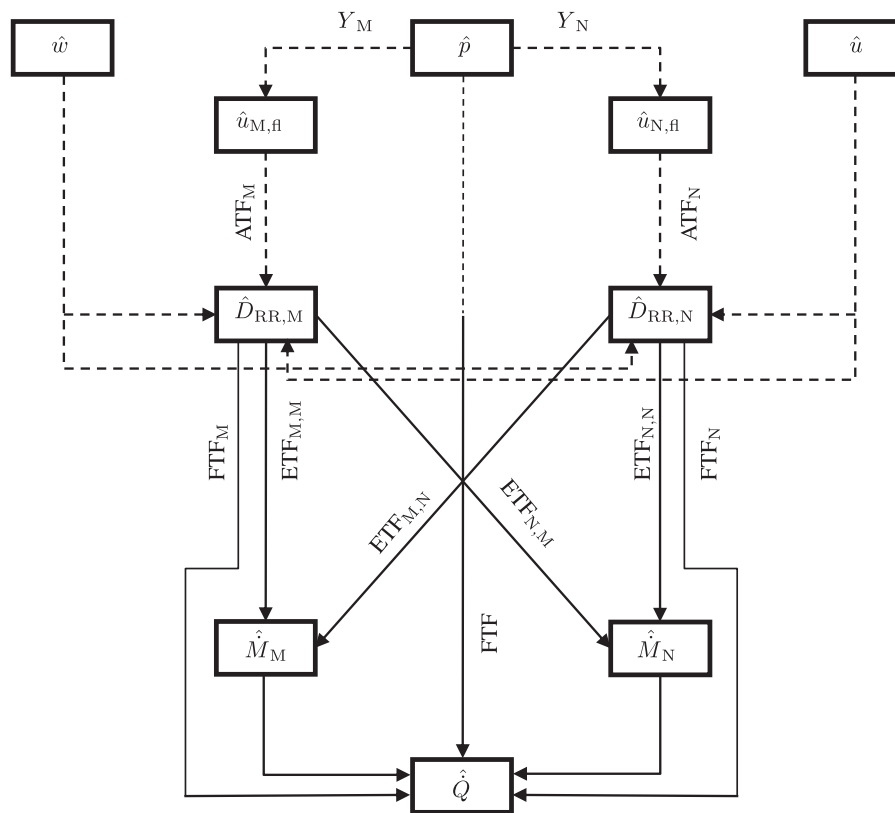

Figure 5. Influence of acoustic fields in hypergolic rocket engines on atomization quality, evaporation, and dynamic heat release in the flame. FTF: flame transfer function; ETF: evaporation transfer function; ATF: atomization transfer function.

varying atomization process, resulting in fluctuating droplet diameter distributions. This is expressed by the fluctuating characteristic diameters of the Rosin–Rammler distribution $\hat{D}_{RR,M}$ and $\hat{D}_{RR,N}$.

The acoustic fluctuations have an impact on the primary as well as on the secondary breakup of the liquid propellant jets, which hardly can be precisely quantified. This problem will be circumvented in the following by assuming a universal law for the influence of velocity on the characteristic diameters of the Rosin–Rammler distribution.

The temporal modulation of the atomization quality leads to the dynamic generation of vapor from the liquid propellants ($\hat{M}_M$ and $\hat{M}_N$), since the evaporation rate of individual droplets depends almost quadratically on their diameter. An additional aspect to be considered is that the oscillating diameter distribution automatically modulates the total number of droplets introduced into the computational domain per time step if the mass flow rate is kept constant. This assumption will be made in the following to study the effects originating from fluctuating atomization independent of the direct dynamic effects from the mass flow fluctuation investigated for the same configuration in Sattelmayer et al.[11,23] It is important to note that it is not per se justified to assume that the dynamics of the evaporation of MMH and NTO are independent of each other.

The third and final phase of the influence of acoustic fields on atomization and the subsequent processes is the modulation of the heat release in the flame by the temporally fluctuating evaporation of MMH and NTO. An important point to be considered is that the dynamics of heat release is not statically linked to the evaporation of the propellants, because in the long non-premixed flames characteristic for rocket motors turbulent mixing of MMH and NTO vapor usually limits the reaction rate.

Framework of linear transfer functions

For the modeling of the dynamic processes introduced above, various transfer functions are introduced in the following, which are determined either analytically or by means of numerical simulations. On the basis of this modeling, a feedback model for wave propagation codes will be assembled, which allows to quantify the heat release fluctuation due to atomization quality fluctuations generated by the acoustic wave field in the combustor.

In the considered injector, the jet breakup is determined by the impingement of two liquid jets. Therefore, the atomization quality is dominated by the injection velocities of the propellants in liquid phase. This allows to take only the effects of fluctuating injection velocities into account in the modeling of breakup of the jets and to omit direct influences of the acoustic field on jet disintegration. If dome coupling is neglected, the feed pressures for both injectors are free of acoustic components and constant. This allows for the characterization of the injector dynamics by the injector admittances Y_M and Y_N.

Equations (14) and (15) describe the modulation of the evaporation rate in dimensionless MMH $\widetilde{M}_M$ and NTO $\widetilde{M}_N$ relative to the pressure fluctuation $\widetilde{p}$ in the combustion chamber, which is the input variable (cp. Figure 5).

$$\widetilde{M}_M = \frac{\hat{M}_M}{\bar{M}_M} = \left(\bar{u}_{M,fl}^{-1} \cdot Y_M \cdot \mathrm{ATF}_M \cdot \mathrm{ETF}_{M,M} \right. \tag{14}$$
$$\left. + \bar{u}_{N,fl}^{-1} \cdot Y_N \cdot \mathrm{ATF}_N \cdot \mathrm{ETF}_{M,N} \right) \cdot \widetilde{p} \cdot \bar{p}$$

$$\widetilde{M}_N = \frac{\hat{M}_N}{\bar{M}_N} = \left(\bar{u}_{N,fl}^{-1} \cdot Y_N \cdot \mathrm{ATF}_N \cdot \mathrm{ETF}_{N,N} \right. \tag{15}$$
$$\left. + \bar{u}_{M,fl}^{-1} \cdot Y_M \cdot \mathrm{ATF}_M \cdot \mathrm{ETF}_{N,M} \right) \cdot \widetilde{p} \cdot \bar{p}$$

A simple analytical model for the admittance of liquid injectors is derived in section Injector admittances for liquid fluids and the admittance values of the MMH and NTO flow paths corresponding to the operating point in Table 1 are given there in addition.

The atomization transfer functions, ATF_M and ATF_N, according to Figure 5 describe the relation between the fluctuation of the injection velocity and the variation of the characteristic diameter of the Rosin–Rammler distribution:

$$\mathrm{ATF}_M = \frac{\widetilde{D}_{RR,M}}{{}_{M,fl}} \tag{16}$$

$$\mathrm{ATF}_N = \frac{\widetilde{D}_{RR,N}}{{}_{N,fl}} \tag{17}$$

Analytical expressions for the modeling of the atomization transfer functions are derived in section Analytical model for the atomization transfer functions.

As evaporation in hypergolic rocket engines is too complex for analytical modeling, the evaporation transfer functions $\mathrm{ETF}_{M,M}$, $\mathrm{ETF}_{N,N}$, $\mathrm{ETF}_{M,N}$, and $\mathrm{ETF}_{N,M}$ in Figure 5 are determined by means of CFD simulations:

$$\mathrm{ETF}_{M,M} = \frac{\widetilde{M}_{M,M}}{\widetilde{D}_{RR,M}} \tag{18}$$

$$\mathrm{ETF_{N,N}} = \frac{\widetilde{\dot{M}}_{N,N}}{\widetilde{\hat{D}}_{RR,N}} \qquad (19)$$

$$\mathrm{ETF_{M,N}} = \frac{\widetilde{\dot{M}}_{M,N}}{\widetilde{\hat{D}}_{RR,N}} \qquad (20)$$

$$\mathrm{ETF_{N,M}} = \frac{\widetilde{\dot{M}}_{N,M}}{\widetilde{\hat{D}}_{RR,M}} \qquad (21)$$

The main goal of these simulations is to reveal the dynamics of the evaporation processes of MMH and NTO and to investigate to which extent the modulation of one of the two droplet diameters influences the evaporation of the other spray. For this purpose, an excitation method is introduced in section Modulation of the atomization quality in the numerical simulations. It is used to obtain well-defined fluctuations of the droplet spectra in the numerical simulations.

Due to the interaction of the evaporation of MMH and NTO, which is expressed in form of the evaporation transfer functions $\mathrm{ETF_{M,N}}$ and $\mathrm{ETF_{N,M}}$ relating the heat release fluctuations to the mass flows of the evaporated propellants $\dot{M}_M$ and $\dot{M}_N$ leads to the problem that each of these quantities depends on both droplet diameters $\hat{D}_{RR,M}$ and $\hat{D}_{RR,N}$. For this reason, the fluctuation of the heat release rate is directly expressed as a function of the two fluctuating droplet spectra $\hat{D}_{RR,M}$ and $\hat{D}_{RR,N}$ according to equation (22). As the consequence, the flame transfer functions (FTF) (23) and (24) cover the dynamics of evaporation, turbulent mixing, and fuel oxidation as well. Comparison of the combined dynamics of these processes with the dynamics of evaporation given by equations (18) to (21) allows to assess to what extent evaporation represents the rate determining step:

$$\widetilde{Q} = \widetilde{\hat{D}}_{RR,M} \cdot \mathrm{FTF_M} + \widetilde{\hat{D}}_{RR,N} \cdot \mathrm{FTF_N} \qquad (22)$$

The FTFs are defined as follows:

$$\mathrm{FTF_M} = \frac{\widetilde{Q}_M}{\widetilde{\hat{D}}_{RR,M}} \qquad (23)$$

$$\mathrm{FTF_N} = \frac{\widetilde{Q}_N}{\widetilde{\hat{D}}_{RR,N}} \qquad (24)$$

Similar to the evaporation transfer functions, both FTFs (23) and (24) are determined from CFD calculations with an imposed fluctuation of the diameter spectrum either of MMH or NTO.

Injector admittances for liquid fluids

Methods for the detailed analysis of the injector dynamics are described for example by Hutt and Rocker Yang and Anderson.[19] In the following, an analytic equation for the injector admittance is presented for the case of liquid propellants. This is possible, provided that the traveling time of the waves within the injector is very short compared to the resonance frequency of the combustion chamber. MMH and NTO have high sonic velocities (on the order of $c \approx 1000 \; \frac{m}{s}$) as they flow through the injector in liquid state. Furthermore, the injector in the considered test case is relatively short (on the order of $L \approx 0.01$ m). Thus, the following estimate for the wave propagation time inside the injector τ_{Inj} can be made:

$$\tau_{Inj} = 2 \cdot \frac{L}{c} = 2 \cdot 10^{-5} \; \mathrm{s} \qquad (25)$$

This time is much smaller than the acoustic period of the first transverse mode of the rocket engine in the focus of the present study $(\approx 3 \cdot 10^{-4} \; \mathrm{s})$. From the time scale comparison follows an almost instantaneous response of the injector mass flows to pressure fluctuations in the combustion chamber.

From steady-state operation, the pressure loss coefficients are determined for both flows in the injector. As the following derivation is valid for both fuel and oxidizer, nomenclature is simplified accordingly.

$$\bar{p}_{Dome} - \bar{p}_{Inj} \approx \bar{p}_{Dome} - \bar{p}_{Comb} = \Delta\bar{p}_{Inj} = \frac{\bar{\rho}_{fl}}{2} \cdot \bar{u}_{fl}^2 \cdot (1+\xi) \qquad (26)$$

Acoustic pressure fluctuations in the combustion chamber influence the velocity at the injector outlet:

$$\bar{p}_{Dome} - (\bar{p}_{Comb} + p') = \Delta\bar{p}_{Inj} - p' = \frac{\bar{\rho}_{fl}}{2} \cdot (1+\xi) \cdot (\bar{u}_{fl} + u'_{fl})^2 = \Delta\bar{p}_{Inj} \cdot \left(1 + \frac{u'_{fl}}{\bar{u}_{fl}}\right)^2 \qquad (27)$$

Furthermore, dome coupling is neglected and a constant dome pressure is assumed. This provides a non-linear relationship between pressure and velocity fluctuations. It is assumed that the pressure loss coefficient is not affected by the acoustic fluctuations:

$$1 - \frac{p'}{\Delta\bar{p}_{Inj}} = \left(1 + \frac{u'_{fl}}{\bar{u}_{fl}}\right)^2 \qquad (28)$$

This is an acceptable assumption for $p' \ll \Delta\bar{p}_{Inj}$. Since the focus of the present study is on linear,

Table 4. Normalized injector pressure drops and injector admittances.

	$\Delta\bar{\tilde{p}}_{\mathrm{Inj,i}}\ [-]$	$Y\left[\frac{\frac{m}{s}}{bar}\right]$
MMH	0.41	−1.47
NTO	0.65	−0.90

MMH: monomethylhydrazine; NTO: nitrogen tetroxide.

spontaneous instabilities, linearization is permitted. After transformation into the frequency domain, the following relationship is obtained:

$$\tilde{u}_{\mathrm{fl}} = \frac{\hat{u}_{\mathrm{fl}}}{\bar{u}_{\mathrm{fl}}} = -\frac{\hat{p}}{2\cdot\Delta\bar{p}_{\mathrm{Inj}}} = -\frac{\hat{p}}{\bar{p}_{\mathrm{Comb}}}\cdot\frac{\bar{p}_{\mathrm{Comb}}}{2\cdot\Delta\bar{p}_{\mathrm{Inj}}} = \\ -\frac{\bar{p}_{\mathrm{Comb}}}{2\cdot\Delta\bar{p}_{\mathrm{Inj}}}\cdot\widetilde{p} \qquad (29)$$

Based on this relationship, the injector admittances for both flow paths of MMH and NTO are given by:

$$Y = \frac{\hat{u}_{\mathrm{fl}}}{\hat{p}} = -\frac{\bar{u}_{\mathrm{fl}}}{2\cdot\Delta\bar{p}_{\mathrm{Inj}}} \qquad (30)$$

For the operating point specified in Table 1, the admittances listed in Table 4 for equations (14) and (15) are obtained.

Analytical model for the atomization transfer functions

As the explicit numerical computation of the disintegration of the injected propellant jets and the subsequent spray formation is beyond reach of the state of the art for the configuration of interest, time mean droplet size distributions and initial conditions are per se assumed (see Table 1) based on past simulation experience with impingement injectors. In the following, an analytical closure model is derived, which describes the modulation of the atomization caused by the acoustic velocities at the injector exit.

Various authors[12,18,19,24] either use the Weber number to characterize the jet breakup and to estimate an average droplet diameter or they provide global analytical relationships between the injection velocity and the average droplet diameter. Using the characteristic droplet diameter of the Rosin–Rammler distribution, D_{RR}, these relationships can be represented as follows:

$$D_{\mathrm{RR}} \propto u_{\mathrm{fl}}^{k} \qquad (31)$$

In the current context of HF oscillations of the atomization quality, the application of equation (31) requires that quasi-steady breakup and spray formation is assumed. This implies that the time scale of the droplet disintegration must be considerably smaller than the acoustic period. Eckstein[20] describes in his work an analogous approach and validates it with experimental data, albeit for a completely different type of injector and for lower frequencies. From equation (31), a non-linear relationship between the fluctuation of the injection velocity and the average diameter of the droplet distribution can be derived:[20]

$$\frac{D'_{\mathrm{RR}}}{\bar{D}_{\mathrm{RR}}} = \left(1 + \frac{u'_{\mathrm{fl}}}{\bar{u}_{\mathrm{fl}}}\right)^{k} - 1 \qquad (32)$$

Linearization and transformation into the frequency domain result in the following relationship:

$$\widetilde{D}_{\mathrm{RR}} = \frac{\hat{D}_{\mathrm{RR}}}{\bar{D}_{\mathrm{RR}}} = k\cdot\frac{\hat{u}_{\mathrm{fl}}}{\bar{u}_{\mathrm{fl}}} = k\cdot_{\mathrm{fl}} \qquad (33)$$

Finally, the introduction of the atomization transfer function according to equations (16) and (17) leads to:

$$\mathrm{ATF} = \frac{\widetilde{D}_{\mathrm{RR}}}{\tilde{u}_{\mathrm{fl}}} = k \qquad (34)$$

Interestingly, the atomization transfer functions are identical with the exponent in equation (31). In the type of injector employed in the current study, jet impingement determines breakup and spray formation. A value of $k \approx -1$ is given in Gill and Nurick[24] for a similar type of injector. As the consequence, the normalized fluctuations of the average diameter and the injection velocity have similar amplitude and they are out of phase by 180°. It is important to note that values of k in that range are not generally valid. Weber number scaling for example does not lead to the same inverse proportionality and for other types of injectors fundamentally different behavior can be found. Even the sign of the exponent may change for other types of atomizers, resulting in in-phase fluctuations of velocity and diameter. Exponents for other types of injectors are given for example in Yang and Anderson.[19] The root cause for the widely scattering exponent depending on the injector type is that the interactions during breakup are rather injector specific. In the case of breakup due to jet impingement, increasing the injection velocity tends to lead to smaller droplets, as the momentum of the jet collision increases. However, for coaxial elements, the shear stresses between the two propellants determine the jet disintegration, which means that an increase of the injection velocity can
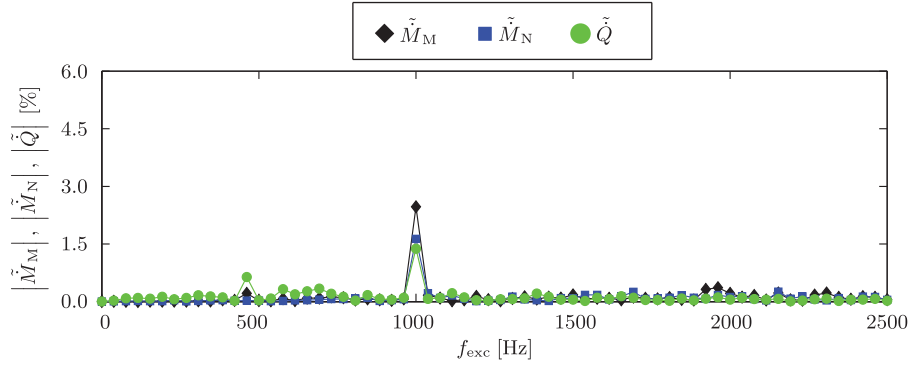
Figure 6. Frequency spectrum (simultaneous excitation of both sprays).

have a stabilizing effect. Inserting equation (30) in equation (34) leads to:

$$\frac{\widetilde{D}_{RR}}{\widetilde{p}} = \frac{\bar{p} \cdot Y \cdot ATF}{\bar{u}_{fl}} = -\frac{k}{2 \cdot \Delta \tilde{\bar{p}}_{Inj}} \qquad (35)$$

It is remarkable that this transfer function depends only on the normalized injector pressure drop. Higher pressure loss makes the feed system stiffer and reduces the influence of acoustic pressure fluctuations in the combustion chamber on jet breakup and spray formation. The pressure losses for the selected operating points and propellants are found in Table 4. For $k = -1$, the droplet sizes oscillate in-phase with the acoustic pressure downstream of the injector.

Modulation of the atomization quality in the numerical simulations

In the two previous sections, analytical models were derived, which allow for the calculation of the atomization quality modulation originating from the acoustic pressure fluctuations downstream of the injector equation (35). However, the subsequent processes are too complex for analytical modeling. For this reason, numerical simulation is applied for the investigation of the influences of the fluctuating characteristic diameters $\hat{D}_{RR,M}$ and $\hat{D}_{RR,N}$ on the evaporation of MMH and NTO, on turbulent mixing, and on heat release. This requires imposing harmonic perturbations on the characteristic droplet diameters of the Rosin–Rammler distribution. Besides the excitation frequency, f_{exc}, the excitation amplitude of the MMH spray $\left|\widetilde{D}_{RR,M}\right|$ and the NTO spray $\left|\widetilde{D}_{RR,N}\right|$, respectively, determines the specific character of the perturbation:

$$D_{RR} = \bar{D}_{RR} \cdot \left(1 + \left|\widetilde{D}_{RR}\right| \cdot \sin(2\pi_{exc})\right) \qquad (36)$$

In the next two sections, the evaporation rates of MMH and NTO as well as the heat release rate are extracted from the individual computations for all excitations and the response in terms of evaporated mass flows and heat release is evaluated in terms of evaporation transfer functions (ETF) and FTF. All results presented in the following were obtained with a perturbation amplitude of 5% for all frequencies.

In Figure 6, the frequency spectra of the evaporation rates of MMH and NTO as well as the heat release rate are shown for simultaneous in-phase excitation of both droplet diameters at $f_{exc} = 1000$ Hz. The evaporation rates of MMH and NTO as well as the heat release rate respond at the perturbation frequency and no significant amplitudes are visible at other frequencies. This indicates linearity for the applied perturbation of 5%. Computations with higher perturbation levels show that the linear behavior is preserved for amplitudes up to 25%. Consequently, the superposition of the transfer functions for simultaneous perturbation of both sprays leads to the same results as simulation with simultaneous excitation for amplitudes below 25%. This also holds if a phase shift between the both spray modulations is applied.

It is interesting to note that the modulation of the evaporation of MMH and NTO is in the same range in terms of amplitudes and that both values are significantly lower than 5%. Apparently, the finite length of the evaporation region prevents full conversion of the fluctuation of the characteristic diameter into evaporation. Most likely due to the large flame length, the heat release fluctuation remains slightly weaker than the modulation of the evaporation rates, although both sprays are simultaneously excited in the computations shown in Figure 6.

Influence of atomization quality modulation on MMH and NTO evaporation

In Figure 5, four transfer functions have been introduced, which relate the dynamics of MMH and NTO
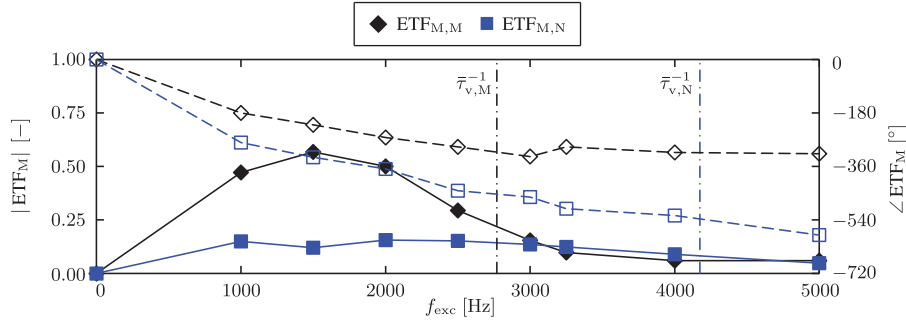
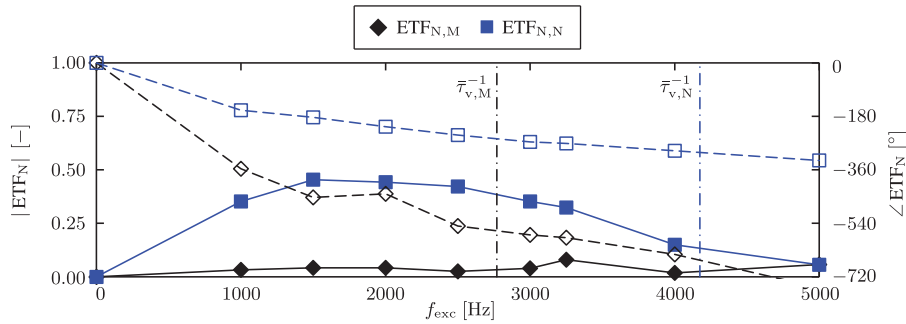**Figure 7.** MMH-evaporation transfer functions (— amplitude, −− phase). ETF: evaporation transfer function.

Figure 8. NTO-evaporation transfer functions (— amplitude, −− phase). ETF: evaporation transfer function.

evaporation ($\hat{M}_M$ and $\hat{M}_N$) to the modulation of the characteristic diameters of the droplet size distributions ($\hat{D}_{RR,M}$ and $\hat{D}_{RR,N}$). In the following, these transfer functions are discussed.

The dimensionless response of the MMH evaporation to an excitation of the characteristic diameter of MMH ($ETF_{M,M}$) and NTO ($ETF_{M,N}$) is shown in Figure 7. The amplitudes are represented by solid and the phases by dashed curves. Both transfer functions start for a vanishingly small frequency at an amplitude of zero, since the integral evaporation mass flow does not change, as long as all droplets fully evaporate without significant time delay. $|ETF_{M,M}|$ has a maximum of 0.57 at a frequency of 1500 Hz. At higher frequencies, the amplitude drops sharply before it remains at a low level of about 0.1. The phase drops with increasing frequency indicating a characteristic time delay.

Qualitatively, the transfer function based on the perturbation of the NTO diameter shows similar behavior. However, the maximum is considerably smaller and almost constant in the frequency range of interest from 1000 to 3000 Hz and the phase drops faster with frequency.

The reason for the influence of the NTO spray on the MMH evaporation is caused by the MMH overshoot in the overall rich flame. Therefore, the heat release fluctuations are dominated by the deficit propellant, which is NTO. Heat release oscillations, in turn, control the

fluctuating evaporation rates. Consequently, the evaporation of MMH by the modulated NTO spray is most likely caused by the periodic heat release from NTO spray modulation.

Table 3 provides average evaporation times for both sprays and the corresponding pseudo-frequencies which are shown in Figure 7 ($\bar{\tau}_{v,M}^{-1}$ and $\bar{\tau}_{v,N}^{-1}$). Characteristic time delays between modulation of characteristics diameters and evaporation can be evaluated by the phase drop, viz.

$$\tau_{M,M/M,N} = \frac{d}{d f_{exc}} \left(\angle ETF_{M,M/M,N} \right) \qquad (37)$$

and are given by $\tau_{M,M} \approx \tau_{M,N} \approx 0.2$ ms for MMH- and for NTO-excitation as well. A comparison to the average evaporation times shows that significant response of the evaporation requires that the characteristic time of the perturbation exceeds the characteristic evaporation times. At the pseudo-frequencies, $\bar{\tau}_{v,M}^{-1}$ and $\bar{\tau}_{v,N}^{-1}$, however, the response is already strongly reduced.

Figure 8 shows the transfer function of the NTO evaporation rate for perturbations of the NTO ($ETF_{N,N}$) and the MMH ($ETF_{N,M}$) spray quality. The very small amplitude in the entire frequency range of $ETF_{N,M}$ indicates that the NTO evaporation is hardly affected by the excitation of the MMH spray.
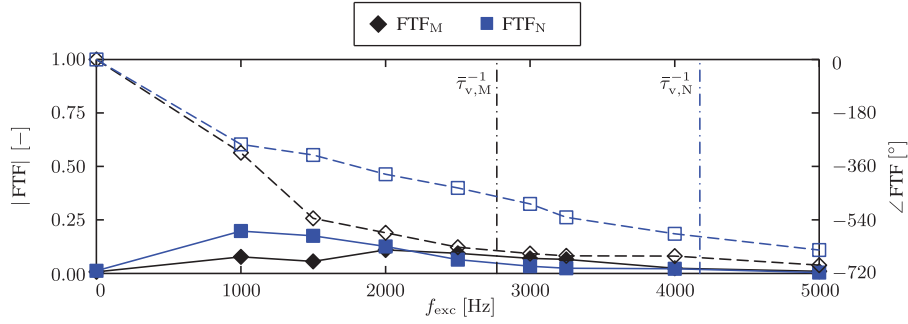
Figure 9. Flame transfer functions (— amplitude, – – phase). FTF: flame transfer function.

This behavior is again explained by the overall rich flame. As the MMH evaporation is not the limiting factor, its dynamics do not play a decisive role for the fluctuating heat release rates.

The comparison with Figure 7 shows that below 2500 Hz the response of the NTO evaporation to the perturbation of the NTO spray $(ETF_{N,N})$ is lower than the sensitivity of MMH evaporation on the perturbation of the MMH spray $(ETF_{M,M})$, but at higher frequencies the opposite is observed. This effect is particularly visible at frequencies between 2500 and 4000 Hz. This behavior can be explained by the different pseudo-frequencies $\bar{\tau}_{v,M}^{-1}$ and $\bar{\tau}_{v,N}^{-1}$. For NTO, this frequency is higher and NTO evaporation response is therefore stronger in the higher frequency range. Particularly, the higher pseudo frequency $\bar{\tau}_{v,N}^{-1}$ of the NTO spray corresponds to faster evaporation. The time delay determined from the phase drop for NTO-excitation and -evaporation is $\tau_{N,N} \approx 0.15\,\text{ms}$. Again, this value is close to the corresponding average evaporation time scale (Table 3).

In summary, the time delays calculated from the phase drops are in all four cases close to the mean evaporation times of the sprays listed in (Table 3). This provides evidence that the dynamics of spray evaporation is governed by the average evaporation times of the sprays. As already explained, a static change of the droplet diameter does not lead to a change in the integral evaporation mass flow. The modulation of the evaporation mass flow with dynamic variation of the droplet diameter is caused by the fluctuation of the droplet surface, which is decisive for the heat and mass transfer between the droplet and the surrounding gas. However, the evaporation rate and the flow field need a certain relaxation time to adapt to the periodically changing droplet diameter. If the period of the excitation is on the order of the relaxation time, a dynamic response of the evaporation rate is observed. However, at periodic times considerably smaller than the relaxation time, the capability to respond is lost.

Influence of atomization quality modulation on heat release

If the MMH and NTO spray qualities are separately perturbed, the two FTFs, FTF_M and FTF_N, are obtained from the numerical study. Both are based on the characteristic diameter of the sprays $\tilde{D}_{RR.M}$ and $\tilde{D}_{RR.N}$, respectively. The results are shown in Figure 9. Only at low frequency, the response is dominated by the influence of the NTO spectrum. This finding can be explained by the overall rich flame. However, at higher frequencies, modulation of the MMH and the NTO spray is similarly effective but the amplitudes are very low. It is likely that this is the result of the large flame length which limits the coherence of the response on the perturbations. Apparently, turbulent mixing and heat release lead to additional dispersion which deteriorates dynamic response and which leads to the strong phase drop of FTF^M and FTF^N visible in Figure 9.

Thermoacoustic flame feedback model

For coupling with the wave propagation code, the FTF is required, which relates the normalized heat release $\tilde{\tilde{Q}}$ to the dynamic pressure $\tilde{p}$ in the complex frequency domain. The global transfer function FTF is illustrated by the vertical arrow in the center of Figure 5. As the pressure fluctuation in the combustion chamber $\tilde{p}$ is the starting point for the modulation of the atomization quality, $\tilde{p}$ is the input variable transferred from the wave propagation code, whereas the output of the feedback model is the normalized heat release $\tilde{\tilde{Q}}$, which appears in the source term of the wave transport equations. On the basis of the framework of linear transfer functions introduced in section Governing effects, the following equation for the FTF is obtained:

$$\text{FTF} = \frac{\tilde{\tilde{Q}}}{\tilde{\tilde{p}}} = \text{FTF}_M \cdot \text{ATF}_M \cdot Y_M \cdot \frac{\bar{p}}{\bar{u}_{\text{fl},M}}$$
$$+ \text{FTF}_N \cdot \text{ATF}_N \cdot Y_N \cdot \frac{\bar{p}}{\bar{u}_{\text{fl},N}} \quad (38)$$
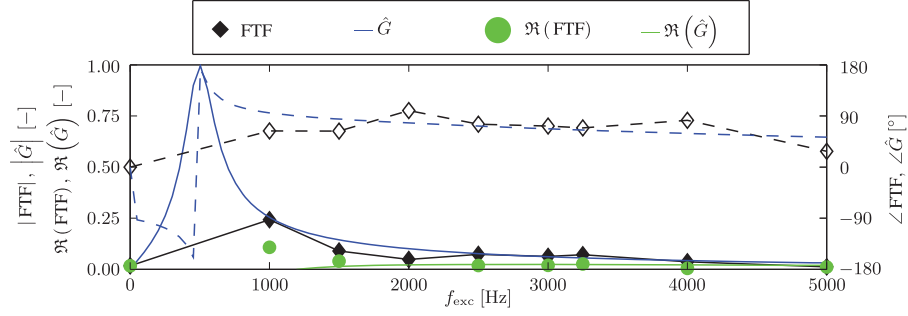
Figure 10. Global flame dynamics and analytical approximation (— amplitude, − − phase). FTF: flame transfer function.

Inserting the analytical models for the injector admittances Y_M and Y_N equation (30) as well as the atomization transfer functions ATF_M and ATF_N equation (34) leads to:

$$\text{FTF} = \frac{\widetilde{Q}}{\widetilde{p}} = \text{FTF}_M \cdot \frac{k}{-2 \cdot \Delta \widetilde{p}_{\text{Inj, M}}} + \text{FTF}_N \cdot \frac{k}{-2 \cdot \Delta \widetilde{p}_{\text{Inj, N}}} \tag{39}$$

Combination of equation (39) with the data for FTF_M and FTF_N from the numerical computations with perturbation of the spray diameters presented in Figure 9 yields the amplitude and phase of the transfer function shown in Figure 10 as black curves. The highest amplitude is present around 1000 Hz. Above this frequency, the amplitude drops and assumes an almost constant value of about 0.05. In the frequency range of interest between around 3250 Hz, the phase is almost constant and slightly below 90°.

Regarding the simple implementation of the feedback model in wave propagation codes, an analytical approximation of the FTF is required. With $f_{LP} = 6000$ Hz, $f_{BP} = 500$ Hz, $B = 200$, and $K = -1.0$, the following combination of a low-bass and a band-pass filter structure delivers the amplitude and phase distributions shown as blue curves in Figure 10:

$$\hat{G}(i\omega) = K \frac{1}{1 + \dfrac{i\omega}{\omega_{LP}}} \frac{i\omega \cdot \dfrac{2\pi}{\omega_{BP}^2}}{1 + i\omega \cdot \dfrac{2\pi}{\omega_{BP}^2} + (i\omega)^2 \cdot \dfrac{1}{\omega_{BP}^2}} \tag{40}$$

Apparently, the filter $\hat{G}(i\omega)$ approximates the transfer function FTF in the frequency range above 1000 Hz with good accuracy. The high amplitude peak of the filter in the range below 1000 Hz may be unphysical but this frequency range is irrelevant in the current context because it is far below the cut-on frequency of the first transverse pulsation mode of the considered rocket engine (≈ 3000 Hz).

Thermoacoustic driving potential of atomization quality fluctuations

The evaluation of the Rayleigh index, Ra, allows for the direct evaluation of the thermoacoustic driving potential of confined flames. This concept is applied to illustrate the thermoacoustic driving potential of atomization quality fluctuations.[2] The Rayleigh index is expressed as follows if the FTF is based on pressure, cp. equation (38):

$$\text{Ra} = \Re(\text{FTF}) \cdot |\widehat{p}|^2 \tag{41}$$

If the heat release fluctuations and the pressure oscillations are in phase, the Rayleigh index is positive and the driving potential is at its maximum. With increasing phase, the driving potential drops and becomes zero for 90° phase angle. For even larger phases, the Rayleigh index becomes negative and combustion dynamics damp oscillations. According to equation (41), the real part of the FTF determines whether atomization quality fluctuations amplify or damp thermoacoustic instabilities in the rocket engine. In Figure 10, the real part of the FTF is represented by the green symbols and the green solid line depicts the real part of the approximation with equation (40).

The positive real part of the FTF in the entire frequency domain indicates that the modulation of the atomization quality by the acoustic field always leads to driving of thermoacoustic instabilities. On the other hand, the real part of the FTF is significantly smaller than its amplitude, because the phase of the FTF is near 90°. This indicates that the driving potential is relatively low and that other types of feedback like direct pressure[2] or velocity[11] coupling or injector mass flow fluctuations[23] may dominate the feedback of the flame to the acoustic field in the type of hypergolic rocket engines investigated in the study.

Conclusions

Flame dynamics are investigated employing an impingement type injector configuration typical for upper stage hypergolic rocket engines propelled by

MMH and NTO. The focus is on the heat release fluctuations originating from the periodic modulation of the atomization quality, which leads to thermoacoustic feedback of the flame on the acoustic field and influences combustion stability accordingly.

Steady state results show that spray interaction and evaporation processes occur within four equivalent injector diameters after injection. A longer flame length observed, however, is explained by subsequent mixing and chemical reaction, showing the complex interplay of all combustion processes, each of which provides distinct characteristic time scales.

A detailed framework of the mechanisms involved is presented linking the interactions of the processes on the basis of linear transfer functions. It consists of three consecutive steps, which are the transformation of the acoustic pressure into fluctuating injection velocity, the perturbation of MMH and NTO spray quality by the fluctuating injection velocity, and the heat release fluctuations originating from the fluctuating spray.

The numerical evaporation study reveals that the frequency range with significant response is limited by the characteristic evaporation times of the sprays. The NTO spray affects the dynamics of MMH evaporation but the NTO evaporation does not show the equivalent effect on MMH evaporation. This lack of symmetry probably stems the global MMH overshoot in the fuel rich flame. The maximum amplitudes of the ETFs are significantly below one, indicating the presence of dispersive effects due to convection in the evaporation zone of finite size.

The amplitudes of the FTFs for MMH and NTO based on the perturbation of the spray quality do not reach the levels of the amplitudes of the ETFs and the flame response becomes very weak at higher frequencies. This illustrates that the dynamics of the evaporation process is only partly converted into heat release fluctuations. Apparently, turbulent mixing and chemical reaction in the long flame zone lead to additional dispersive effects.

The estimation of the thermoacoustic feedback of the periodic modulation of the atomization quality on the basis of the Rayleigh index provides evidence for certain driving potential, but the phase angle between pressure and heat release fluctuation near $90°$ indicates that it might be limited. Since several other feedback mechanism is also present in reality, the contribution of the modulations of the atomization quality in both sprays to the overall driving potential of the flame might be of minor importance. To ultimately study the relevance of atomization dynamics for thermoacoustic stability with wave propagation codes, a feedback model is derived on the basis of analytical models and dynamics CFD results.

Declaration of conflicting interests

The author(s) declared no potential conflicts of interest with respect to the research, authorship, and/or publication of this article.

References

1. Morgenweck D, Fassl F, Kaess R, et al. Influence of Scaling Rules on Loss of Acoustic Energy. *J Spacecraft and Rockets* 2011; 48: 498–506.
2. Schmid M. *Thermoacoustic Feedback Phenomena in Liquid Rocket Engines*, Ph.D. thesis, Institute for Thermodynamics, Technical University of Munich, 2014.
3. Schmid M and Sattelmayer T. Influence of pressure and velocity perturbations on the heat release fluctuations for coaxial GH2/GO2 injection. In: *4th European conference for aerospace sciences*, St. Petersburg, Russia, 2011.
4. Schmid M and Sattelmayer T. Interaction of acoustic pressure fluctuations with supercritical nitrogen jets. In: *48th AIAA/ASME/SAE/ASEE joint propulsion conference & exhibit*, Atlanta, Georgia, USA, 2012, AIAA 2012–3858.
5. Schulze M, Schmid M, Morgenweck D, et al. A conceptional approach for the prediction of thermoacoustic stability in rocket engines. In: *49th AIAA/ASME/SAE/ASEE joint propulsion conference*, San Jose, California, USA, 2013, AIAA 2013–3779.
6. Pieringer J. *Simulation of Self-Excited Combustion Instabilities in Rocket Engines in Time Domain*, Ph.D. thesis, Institute for Thermodynamics, Technical University of Munich.
7. Crocco L and Cheng S. *Theory of combustion instability in liquid propellant rocket motors*. London: Butterworths Scientific Publications, 1956.
8. Culick FEC. Combustion instabilities in liquid fueled propulsion systems - an overview. AGARD-CP 450, 1988.
9. Culick FEC. Unsteady motions in combustion chambers for propulsion systems. AC/323(AVT-039)TP/103, RTO AGARDograph, 2006.
10. Schulze M, Urbano A, Zahn M, et al. Thermoacoustic feedback analysis of a cylindrical combustion chamber under supercritical conditions. In: *50th AIAA/ASME/*

SAE/ASEE joint propulsion conference, Cleveland, Ohio, USA, 2014, AIAA 2014-3776.

11. Sattelmayer T, Schmid M and Schulze M. Interaction of combustion with transverse velocity fluctuations in liquid rocket engines. *Journal of Propulsion and Power* 2015a; 31: 1137–1147.

12. Lefebvre AH. *Atomization and sprays*. New York, NY: Hemisphere Publishing Corp., Combustion, 1989.

13. ANSYS Inc. *ANSYS CFX-solver theory guide – ANSYS CFX release 14.0*. Canonsburg, PA: ANSYS, 2011.

14. Knab O, Fröhlich A and Wennerberg D. Design support for advanced storable propellant engines by ROCFLAM analyses. In: *35th AIAA/ASME/SAE/ASEE joint propulsion conference and exhibit*, 1999.

15. Knab O, Preclik D and Estublier D. Flow field prediction within liquid film cooled combustion chambers of storable bi-propellant rocket engines. In: *34th AIAA/ASME/SAE/ASEE joint propulsion conference and exhibit*, 1998.

16. Aichner T, Riedmann H, Kniesner B, et al. Development of an advanced global MMH/NTO combustion model for CFD application. In: *Space propulsion AAAF-ESA-CNES*, No. 2356608, 2012.

17. Schmid M. *Modelling of film cooling and decomposition in MMH/NTO rocket engines*. Masters' Thesis, EADS Astrium/TU Kaiserslautern/INSA Rouen, 2009.

18. Joos F. *Technical Combustion*. Limited Edition. London: Springer, 2007.

19. Yang V and Anderson WE. *Liquid rocket engine combustion instability*. University Park, PA: American Institute of Aeronautics and Astronautics, 1995.

20. Eckstein J. *On the mechanisms of combustion driven low-frequency oscillations in aero-engines*. PhD Thesis, Lehrstuhl für Thermodynamik, Technische Universität München, 2005.

21. Ganji A and Dunn-Rankin D. Spray modulation with potential application in gas turbine combustors. In: *32nd joint propulsion conference and exhibit*, 96-2625, 1996.

22. Takahashi F, Schmoll WJ and Dressler JL. Characteristics of a velocity-modulated pressure-swirl atomizing spray. *Journal of Propulsion and Power* 1995; 11: 955–963.

23. Sattelmayer T, Schmid M and Schulze M. Impact of injector mass flow fluctuations on combustion dynamics in liquid engines. *Journal of Spacecraft and Rockets* 2015b; 52: 1417–1429.

24. Gill GS and Nurick WH. *Liquid rocket engine injectors*. NASA SP 8089, 1976.

Appendix

Notation

A_{EDC}	prefactor (Eddy Dissipation model)	–
A_{FR}	prefactor (Finite Rate model)	s^{-1}
B	band width	–

(continued)

Continued

B	Antoine parameter	K
C	Antoine parameter	K
c	Speed of sound	m/s
D_D	Droplet diameter	Mm
D_F	Diffusivity	m^2/s
D_{RR}	Characteristic droplet diameter	μm
E	Activation energy	J/kg
f	Frequency	1/s
f_v	Volume-based droplet distribution	1/m
G	Filter	–
h_v	Enthalpy of evaporation	kJ/kg
k	Exponent	–
k_t	Turbulent kinetic energy	J/kg
K	Filter proportionality constant	–
L	Length	m
$\dot{M}$	Mass flow rate	kg/s
Nu	Nusselt number	[–]
n	Exponent (Rosin–Rammler distribution)	–
O/F	Oxidizer to fuel ratio	–
p	Pressure	Pa
p_{sc}	Antoine pressure	Pa
$\dot{Q}$	Heat release rate	W
R	Radius	m
$\mathcal{R}$	Gas constant	J/kg/K
$R^\star$	Reference radius	m
Ra	Rayleigh index	$W \cdot Pa$
Re	Reynolds number	[–]
Sh	Sherwood number	[–]
s	Spectral variable	rad/s
T	Temperature	K
u	Axial velocity	m/s
x	Axial coordinate	m
Y	Admittance	m/s/Pa
Y_i	Mass fraction of i-th component	
w	Transverse velocity	m/s
W	Molar mass	kg/kmol
α	radial injection angle	rad
β	Temperature exponent of Finite Rate model	–
ϵ	Turbulent dissipation rate	m^2/s^3
λ_Q	Heat conductivity	W/m/K
μ	Dynamic viscosity	Pa·s
ν_i	Stoichiometric coefficient of i-th component	–
ρ	Density	kg/m^3
τ	Characteristic time	s
τ_v	Evaporation time	s
χ	Mole fraction	[–]
ω	Angular frequency	rad/s
$\dot{\omega}$	Species source term	$kg/m^3/s$

(continued)

Continued		
ξ	Pressure loss coefficient	–
$()_{BP}$	Band pass	
$()_{Comb}$	Combustion chamber	
$()_{Dome}$	Dome	
$()_{exc}$	Excitation	
$()_{fl}$	Fluid (liquid)	
$()_{Inj}$	Injector	
$()_{i}$	Inner	
$()_{LP}$	Low pass	
$()_{M}$	MMH, Monomethylhydrazine	
$()_{N}$	NTO, Nitrogen tetroxide	

(continued)

Continued	
$()_{o}$	Outer
$()_{R}$	Reactants
$()_{\theta}$	Circumferential
$\widetilde{()}$	Dimensionless quantity
$\overline{()}$	Mean value
$\widehat{()}$	Complex amplitude
$()'$	Fluctuation
$()_{s}$	Equilibrium
$()_{v}$	Vaporization
$\Re$	real part